Author/s:
Li, N;Cadusch, J;Liu, A;Barlow, AJ;Roberts, A;Crozier, KB

Title:
Algorithm-Designed Plasmonic Nanotweezers: Quantitative Comparison by Theory, Cathodoluminescence, and Nanoparticle Trapping

Date:
2021-10-01

Citation:
Li, N., Cadusch, J., Liu, A., Barlow, A. J., Roberts, A. & Crozier, K. B. (2021). Algorithm-Designed Plasmonic Nanotweezers: Quantitative Comparison by Theory, Cathodoluminescence, and Nanoparticle Trapping. Advanced Optical Materials, 9 (19), https://doi.org/10.1002/adom.202100758.

Persistent Link:
https://hdl.handle.net/11343/294845

Title
Algorithm-designed plasmonic nanotweezers: quantitative comparison by theory, cathodoluminescence and nanoparticle trapping

Authors
Neuton Li, Jasper Cadusch, Amelia Liu, Anders J. Barlow, Ann Roberts, Kenneth B. Crozier**

Neuton Li
Research School of Physics, Australian National University, Canberra, Australian Capital Territory, Australia 2600
School of Physics, University of Melbourne, Victoria 3010, Australia
E-mail: neuton.li@anu.edu.au

Dr. Jasper Cadusch, Prof. Kenneth Crozier
Department of Electrical and Electronic Engineering, University of Melbourne, Victoria, 3010, Australia

Dr. Amelia Liu
School of Physics and Astronomy, Monash University, Clayton, Victoria 3800, Australia

Dr. Anders Barlow
Materials Characterization and Fabrication Platform, University of Melbourne, Victoria 3010, Australia

Prof. Ann Roberts, Prof. Kenneth Crozier
School of Physics, University of Melbourne, Victoria, Melbourne, Australia 3010
ARC Centre of Excellence for Transformative Meta-Optical Systems (TMOS), University of Melbourne, Victoria 3010, Australia
E-mail: kenneth.crozier@unimelb.edu.au

Keywords: optical tweezers, plasmonics, algorithm designs, nanophotonics

Abstract: Plasmonic apertures permit optical fields to be concentrated into sub-wavelength regions. This enhances the optical gradient force, enabling the precise trapping of nanomaterials such as quantum dots, proteins, and DNA molecules at modest laser powers. Double nanoholes, coaxial apertures, bowtie apertures, and other structures have been studied as plasmonic nanotweezers, with the design process generally comprising intuition followed by electromagnetic simulations with parameter sweeps. Here we instead use a computational algorithm to design plasmonic apertures for nanoparticle trapping. The resultant apertures have highly irregular shapes that, in combination with ring couplers also optimized by algorithm, are predicted to generate trapping forces more than an order of magnitude greater than those from

the double nanohole design used as the optimization starting point. We realize our designs by fabricating precision apertures with a helium/neon ion microscope and study them by cathodoluminescence and optical trapping. We show that, at every laser intensity, the algorithm-designed apertures can trap particles more tightly than the double nanohole.

1. Introduction

Optical tweezers enable study of the motion and dynamics of particles in a non-invasive manner and with high precision.[1–5] The ability to manipulate individual nanoparticles in a non-contact manner at ever lower laser powers is advantageous for the rapidly expanding field of nanoscience, enabling observations to be performed over extended periods and potentially forming the foundation for a nanoscale assembly tool. The optical trapping of nanoparticles faces the challenge however that the gradient force varies approximately with the nanoparticle volume.[6–8] This means, for example, that reducing the nanoparticle radius by a factor of ten reduces the gradient force by a factor of one thousand. As the name suggests, this force also varies with the gradient of the intensity. One can therefore boost the gradient force by concentrating light as tightly as possible at the trapping site. Conventional optical tweezers however use lenses to focus light and are thus subject to the diffraction limit. This sets a limit on the gradient force on a given nanoparticle that can be obtained with a given laser power with conventional optical tweezers.[9]

Optical nanostructures enable optical fields to be concentrated into deeply-sub wavelength regions, thereby presenting a means to surpass the performance of traditional optical tweezers for the trapping of nanoparticles. Optical tweezers based on nanostructures are sometimes known as optical nanotweezers. Plasmonic apertures have proven highly effective,[10–17] with the enhanced fields inside the apertures producing strong gradient forces.[18] The presence of heating is an important consideration in optical nanotweezers. In some cases it can be an advantage,[19] though generally it is considered detrimental. Optical nanotweezers based on

plasmonic apertures benefit from the fact that the contiguous metal film serves as a heat-sink,[12,20] a mechanism that has been also used in other optical nanotweezer types.[21] Other advantages include the ability to readily observe trapping events via changes in optical transmission,[22] the enhancement of the force that can occur via particle-aperture interactions dubbed the self-induced back action effect,[23,24] and the fact that their fabrication is relatively straightforward. Various aperture shapes have been investigated as optical nanotweezers,[23] including circular nanoholes,[19,25,26] rectangular nanoholes,[22] coaxial apertures,[10,13] bowtie apertures,[27–29] asymmetric split rings,[30] connected nanorings,[31] C-shaped apertures,[32,33] and double nanoholes.[12,14,15,20,34–37] Thus far, the design process has generally consisted of physical intuition (to choose, for example, the nanoaperture shape) followed by electromagnetic simulations (e.g. to optimize dimensions). This presents the question of whether an algorithm could design a nanoaperture for optical nanotweezers with superior performance. We recently investigated this via a simulation-only study.[38] Here, we study this by experiment and employ our algorithm to design nanoapertures for trapping. These have highly irregular shapes and are combined with concentric rings that serve as couplers, also optimized by algorithm. We use a helium/neon ion microscope to fabricate these designs with high precision. These structures are characterized using cathodoluminescence and employed for nanoparticle trapping. We show that at every laser intensity, the algorithm-designed structures trap particles more tightly than a nanoaperture shape that has been widely employed for optical nanotweezers, the double nanohole.

Our approach is motivated by the clear benefits of optimization algorithms and machine learning that have been demonstrated in other areas of optics and photonics. Some examples are as follows. Shen et al used a nonlinear optimization algorithm to design a beamsplitter with a footprint (of $2.4\times2.4\ \mu m^2$), making it the smallest beamsplitter that had been demonstrated.[39] Jiang and Fan demonstrated a global optimizer based on a neural network that could extensively search parameter space, shifting to favorable design space regions.[40] They

applied this tool to design metagratings that operated over a range of wavelengths and angles. Chung and Miller recently used inverse design to devise metalenses with a variety of numerical apertures (NA). Their low NA devices showed the highest efficiencies to date, while those with high NA were the first to exhibit achromatic focusing.[41] Here we experimentally demonstrate, for the first time to our knowledge, an optical nanotweezer designed by algorithm.

2. Results

2.1. Algorithmic Design

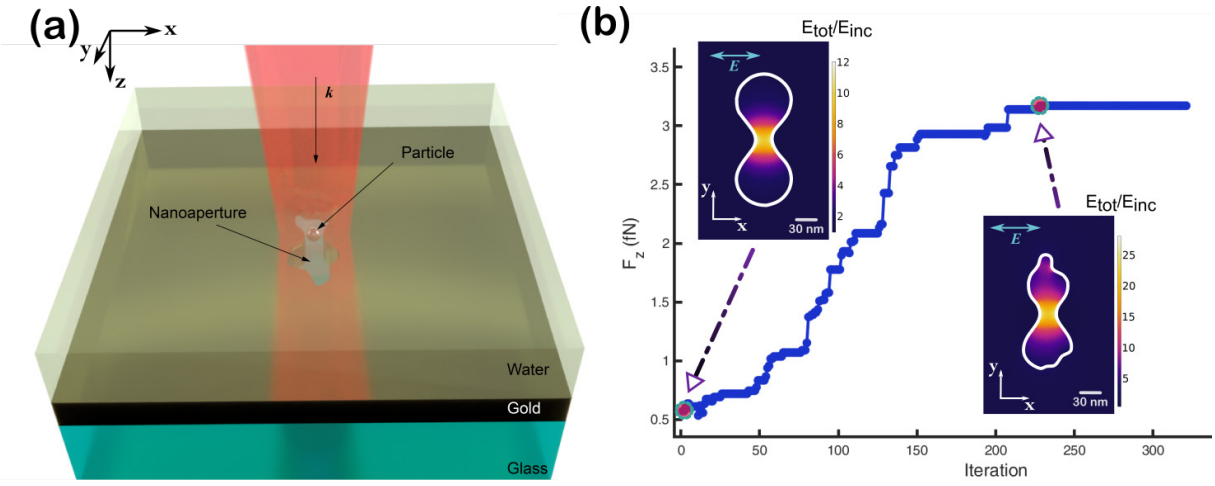

Figure 1: Using algorithms coupled with electromagnetic simulation to increase the efficacy of plasmonic traps. (a) Schematic of particle trapping experiment. Aperture is milled into gold film. Illumination is focused beam (x-polarized, λ=1064 nm) from water side, with focal point at aperture. (b) Force (in z-direction, i.e. into aperture) experienced by particle vs iteration number of optimization algorithm. Particle has refractive index n=1.6 and diameter d=10 nm. Field distributions are shown for design used in first step of algorithm (double nanohole, DNH) and for optimal design (SA2).

We next outline our algorithmic design approach. This implements a simulated annealing algorithm in a custom code (in MATLAB) that also calls a commercial finite element method package (COMSOL Multiphysics) to solve Maxwell's equations. Our device consists of a gold film (100 nm thick) on a glass substrate, into which apertures and concentric rings are formed. The particles to be trapped are in the water above the gold. The algorithm designs an aperture geometry that maximizes the downward force $\boldsymbol{F}_z$ that a particle will experience when in the vicinity of the aperture (**Figure 1**a). In other words, the algorithm optimizes for a figure of merit (FOM) that consists of $\boldsymbol{F}_z$ when the particle (d=10 nm, refractive index n=1.6) is centered over

the nanoaperture and with its center level with the gold surface. This FOM is selected as it is thought to best encapsulate the purpose of plasmonic nanotweezers; namely to draw particles from water into the aperture, then to hold them there stably. We note that the inclusion of a particle near the aperture may cause a self-induced back action (SIBA) effect that can increase the field in the aperture.[23,26] The FOM defined as above will incorporate this phenomenon. Illumination is via a focused beam (numerical aperture NA=1.3) from the water side with a wavelength at 1064 nm that is centered on the aperture. The polarization is linear and across the aperture gap. Calculation of the force is performed by integrating the Maxwell stress tensor over the particle, from which we extract the *z* component of the force as the FOM.

We use the metaheuristic simulated annealing algorithm to find the structure that maximizes the FOM.[42,43] Our algorithm takes as its starting point the double nanohole (DNH), as this design has proven popular for nanoaperture tweezers, having been used by at least four different research groups.[14,15,20,23] The algorithm then iterates by perturbing the boundary of the shape and re-calculating the FOM each time. As with many optimization algorithms, multiple points exist at which the FOM is large, and these FOMs take similar values. Empirically, we find that for most of these points, the nanoapertures are asymmetric. We therefore do not enforce symmetry in the algorithm. To prevent the optimization algorithm from becoming stuck in local optima, we constantly perturb the structure and implement a non-zero probability of accepting structures with inferior performance. Many optimization runs are performed with the same algorithm parameters. The final designs produced by these runs are different due to the randomness of the process, but they exhibit similar performance.

After aperture optimization, we next use the algorithm to optimize a structure that we term a ring coupler. This consists of two broken concentric rings that surround the aperture to aid heat dissipation by keeping the gold film contiguous. This further enhances the FOM because the rings facilitate the coupling of fields into the aperture. More details of the algorithm can be found in Reference [38] and in the Methods section. We note the difference between this

structure to that our work in Reference [38]. Previously, the optimization maximized the local field enhancement in the gap, while in this work, the optimization maximizes the pulling force of the aperture into its centre F_z. The same simulated annealing algorithm was used for both works but optimizing for different quantities.

From Figure 1b, it can be seen that, as the algorithm progresses, $\boldsymbol{F}_z$ increases from its starting value of ~0.5 fN to be in excess of 3 fN at its conclusion. For these simulations, the illuminating intensity is 6.67 mW μm^{-2}. The progression in $\boldsymbol{F}_z$ represents a six-fold increase in the downward force on the particle, which is substantial. In the inset of Figure 1b, we show the electric field enhancement (EFE) on an *xy* plane halfway through the gold film (at z=50 nm) for the initial and final structures. The greatest EFE is in the region of the narrow gap, and we note that the maximal EFE is more than doubled through the optimization. Inclusion of the separately optimized concentric rings leads to a further doubling of the predicted force on a particle. For the resultant structure, therefore, the force on the particle is more than an order of magnitude greater than that of the starting DNH design.

2.2. Design Realization

We use a helium ion microscope (HIM) to mill the optimized apertures into the gold film (**Figure 2**). The milled designs are the simulated annealing aperture (SA) from Reference [38], our special aperture from this work (SA2), also optimized with the simulated annealing, and a double nanohole (DNH). Simulations of the SA and SA2 structures show that they offer similar trapping performance. As discussed, the inclusion of concentric rings (Figure 2a) can further increase the EFE (and the force) in the aperture.[38] We mill arrays of the different apertures with and without rings to characterize the trapping performance of each combination. The rings are milled with the neon ion capability of our system. The devices are well separated (30 μm) to reduce coupling effects. The round edges and oblique walls of the real holes would likely reduce the local field enhancement. We anticipate similar impacts on the DNH and optimized

structures. Because it is very difficult to characterize these accurately, we did not include them in the simulation model used for optimization.

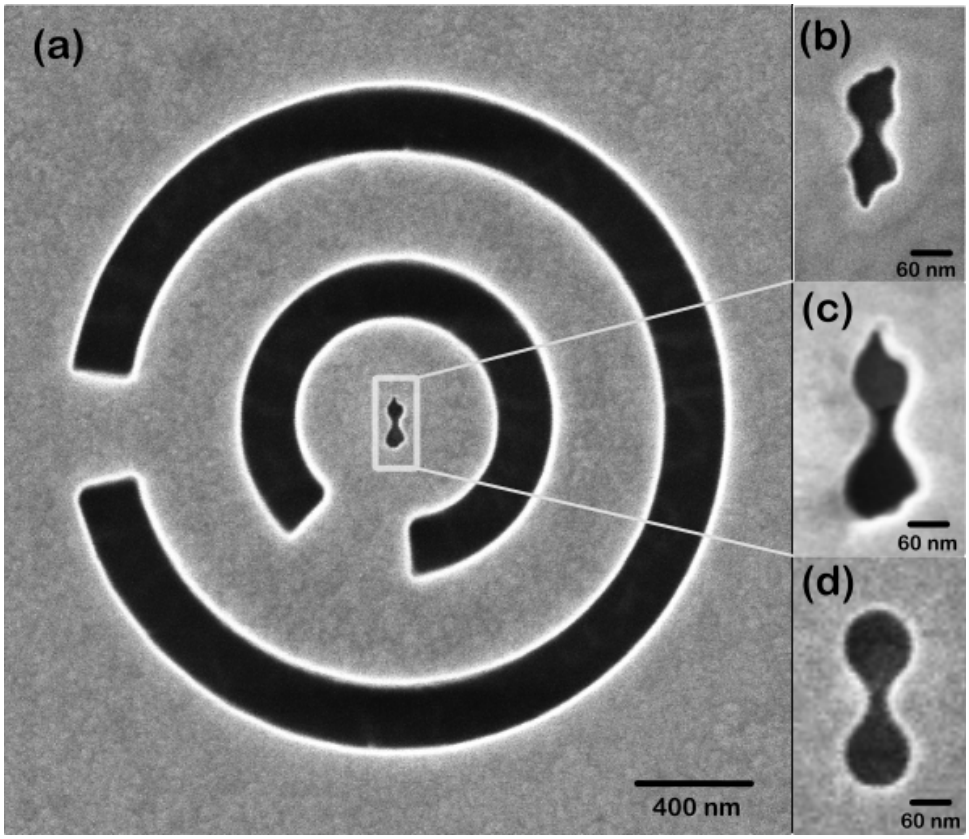

Figure 2: HIM images of the fabricated devices. (a) Device SA2 with concentric rings etched around it, (b) device SA, (c) zoom in of (a), (d) device DNH.

Images collected in the HIM indicate that the fabricated devices have high fidelity to the desired designs, with the very fine details of the shape being produced as desired (**Figure S1**). A microfluidic chamber is created around the aperture (**Figure 3**a) by attaching a glass coverslip (150 μm thick) with a photoresist film (6 μm thick) patterned with a rectangular opening. This creates a thin water chamber in which fluorescent nanoparticles (FluoSphere 20 nm diameter, Life Technologies, nominal diameter d=27 nm) are suspended. The nanoparticles are injected into the chamber via thin hollow polyethylene tubes which protrude through holes drilled into the glass slide. The assembly is kept watertight and flow of water in the cell is avoided, as this may hinder the trapping process. The assembly is mounted onto the microscope in our optical setup (Figure 3b), which is further described in the Methods section.

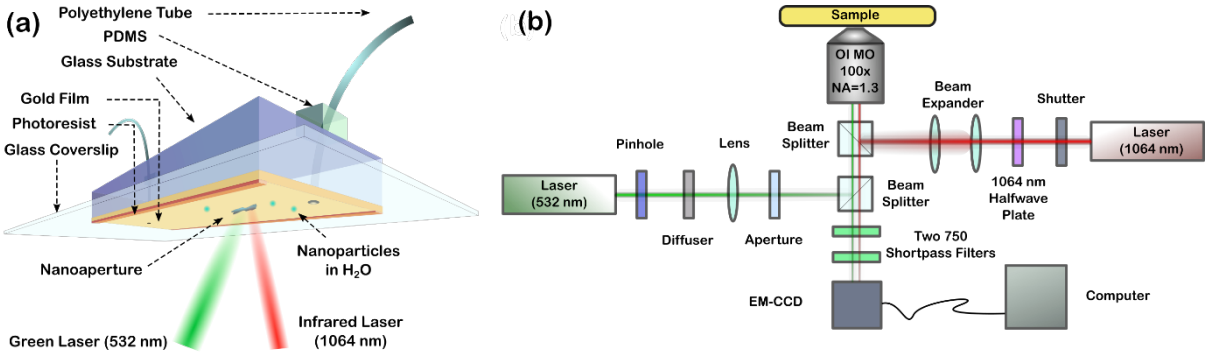

Figure 3: Diagrams of the fluid cell and experimental setup. (a) Schematic of the microfluidic chamber containing the nanoparticles. (b) Schematic of the experimental components and configuration.

2.3. Cathodoluminescence

An energetic electron beam incident on the surface of a material can excite coherent and incoherent processes in the material causing emission of light, a process known as cathodoluminescence (CL).[44] In a scanning electron microscope (SEM) or a scanning transmission electron microscope (STEM) equipped with the CL capability, a focused electron beam is raster scanned over the surface of the specimen with emitted light collected into a spectrometer.[45,46] Incoherent CL, usually generated by electron-hole recombination, has been used to examine strain, defects, and inter-band transitions in nanoscale semiconductors.[47] Coherent CL, so-called because the emitted radiation has a constant phase relation with the electric field of the incoming electron, has mapped LSP resonances in coupled plasmonic systems produced by various methods, including chemical growth and electrostatic assembly,[48,49] electron beam lithography,[50,51] and ion beam milling.[52,53]

Simulations are performed in COMSOL Multiphysics to gain insight into the CL measurements. We model the electron beam with a point dipole source placed just above the surface of the gold. The dipole is oriented along the z-axis, i.e. perpendicular to the plane of the surface.[53] The far-field energy radiated into an approximately hemispherical region surrounding the aperture is calculated. The angular extent of this simulated region is chosen to match that of the collecting mirror in the experiment (NA=0.95). We then scan the dipole position in the x-y plane throughout the domain, including over the milled apertures. We plot the integrated

radiated power at the wavelengths of interest for each dipole position to create each CL intensity map (**Figure 4**). In an analogous fashion, the CL experimental measurements are performed by scanning the electron beam across the domain and collecting the CL spectrum at each position. Further detailed discussion of the CL measurement acquisition, and data processing is provided in the Methods section.

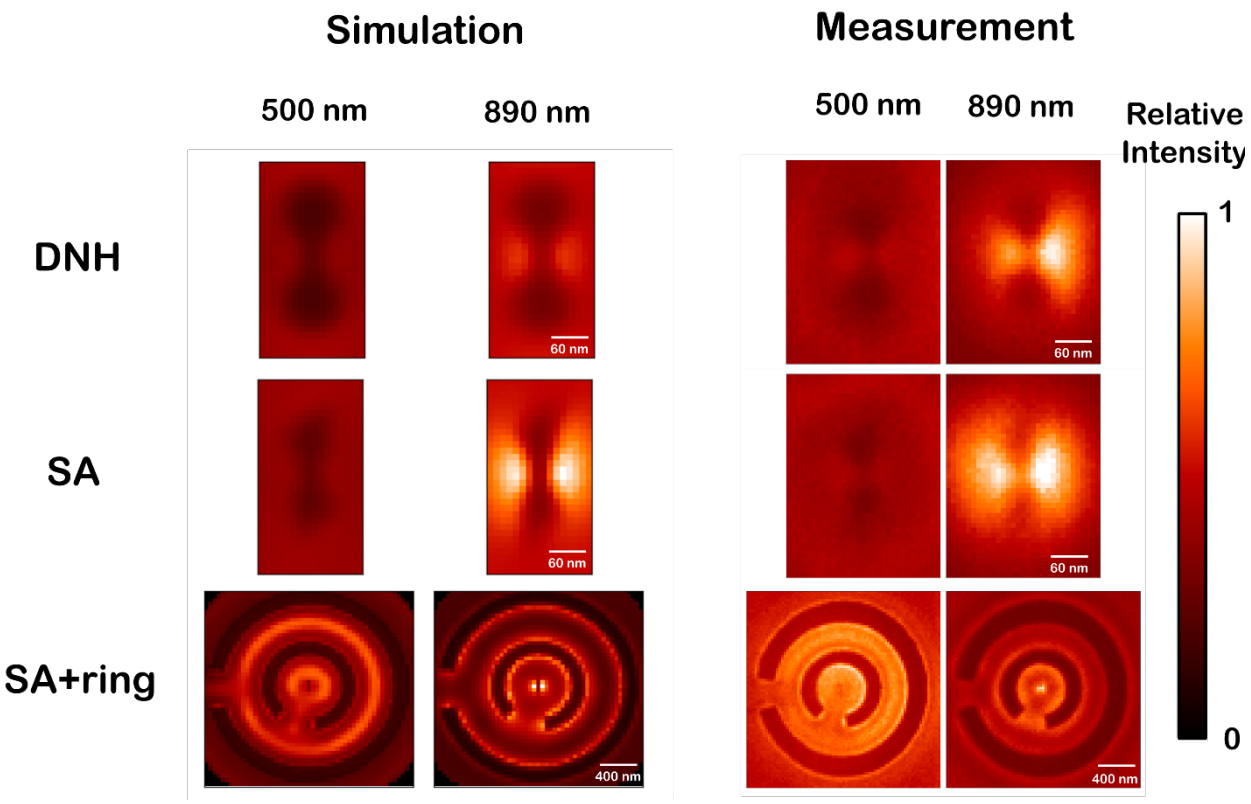

Figure 4: Simulated and measured cathodoluminescence spectral intensity maps at wavelengths of λ =500 nm and 890 nm for the different devices under consideration.

As discussed, in experiments we measure the CL emission spectrum from each position as the electron beam is scanned over the sample. To facilitate interpretation of these results and their comparison to simulations, in Figure 4 we present simulated and measured intensity maps at wavelengths of 500 nm and 890 nm. In addition, a high-resolution CL is map is produced for SA2 (**Figure S2**). Two wavelengths are chosen to allow the results for off-resonance (i.e. 500 nm) and on-resonance (i.e. 890 nm) operation to be compared. We take $\lambda = 890\,nm$ as representing on-resonance operation because the simulated CL emission spectrum near the gap (**Figure S3**) has a peak at λ=890 nm. As discussed, the optimization is performed at a free space

wavelength of λ=1064 nm. The wavelength of the peak in the simulated CL spectrum (λ=890 nm) is therefore close to the effective wavelength in water of the illumination used in the optimization algorithm (i.e. 1064 nm/1.33 = 800 nm). These maps provide insight into the localized surface plasmon (LSP) resonant modes of the apertures.[54] To reduce the effect of noise, the measured CL emission is integrated over a 50 nm bandwidth about the center wavelength (i.e. of 890 nm or 500 nm) to produce each map. For the simulated maps, results for the selected wavelength (i.e. 890 nm or 500 nm) are shown.

Both the simulated and experimental spectra (Figure S3,4) and maps (Figure 4) show that the main LSPR in this spectral range is the dipole mode across the gap and that this is excited more strongly as the electron beam approaches the aperture edge in the gap region. We observe in simulation (Figure 4, **Figure S5**) that at 890 nm, the optimized apertures produce stronger emission than the DNH. This is consistent with the higher EFE that we see in simulations of the optimized structures. However, in experiment, CL emission from SA is only marginally stronger than that from the DNH. One may therefore expect that the trapping force provided by the fabricated optimized aperture (SA) will be greater than that for the DNH, though not as pronounced as expected from simulation. We note that this insight into the expected trapping performance (in water) is provided by the CL measurements, despite the fact that these measurements are performed in vacuum. From **Figure S4**, it can be seen that the CL spectra measured from the SA and DNH peaks are at wavelengths of $\lambda \approx 820$ nm and 830 nm respectively. By contrast, in the simulated CL spectra (Figure S3a) the SA and DNH designs peak at wavelengths of $\lambda \approx 890$ and 1050 nm, respectively. It therefore appears that the resonance of the fabricated DNH structure ($\lambda \approx 830$ nm) is much closer to the wavelength at which the CL map is plotted ($\lambda \approx 890$ nm) than expected from simulations ($\lambda \approx 1050$ nm). Indeed, the measured resonance for the DNH ($\lambda \approx 830$ nm) is closer to $\lambda \approx 890$ nm than the measured resonance of the SA ($\lambda \approx 820$ nm). This might account for the differences between the simulated and measured CL maps ($\lambda \approx 890$ nm) of Figure 4. The underlying reason for this

behavior is not completely clear at this point. As discussed, the fabricated apertures appear to have geometries that match those of the designs (Figure 2 and Figure S1). It is possible that there are differences either in material properties (gold permittivity, especially due to the redeposited gold from helium ion-beam fabrication) or in aperture geometry (e.g. roundedness of corners) that cannot be discerned from top down HIM images (Figure 2 and Figure S1). Our CL measurements reveal differences between simulations and measurements on the position of spectral peaks that would not be predicted from top-down ion beam images. We therefore anticipate that despite the fact that they are performed in vacuum, while optical nanotweezers generally operate in water, CL measurements might also provide valuable insight into other optical nanotweezer designs.

It can be seen that the simulated CL map for the SA + ring structure at 890 nm predicts enhanced emission around the ring edges and around the aperture. This is confirmed by the experimental results. In comparison, at 500 nm, the emission around the rings is weaker and emission maximum does not occur not at the ring edges, but rather in between the rings. This suggests that at resonance, the rings scatter the plasmons in such a way that they form a central interference maximum at precisely the radii of the rings from the center. The result is a stronger coupling of the incident power into the central aperture.

As discussed above, the simulated DNH has a resonance further into the infrared, i.e. it is off-resonance at the operating wavelength (1064 nm). Since a DNH design of this geometry has been used for trapping at 1064 nm in previous works,[15] we use this as a starting point for our optimization algorithm. It is then natural to compare our optimized apertures SA with this DNH. This leads to the question of whether the optimization algorithm is solely performing resonance shifting. As we discuss later in detail, while the algorithm does indeed perform resonance shifting if required, this is not its only function. Indeed, as we discuss later, if the optimization algorithm is run at a longer wavelength (that matches the resonant wavelength of the DNH), it can again yield optimized apertures producing EFEs that surpass those of the starting DNH. We

also show later that our algorithm-designed apertures out-perform a DNH re-designed so that it is resonant at a wavelength of 1064 nm.

2.4. Particle Detection and Trapping

Our experimental set-up (Figure 3b) allows direct observation of individual nanoparticles trapped by a plasmonic nanoaperture via fluorescence microscopy with an electron-multiplying charge coupled device (EMCCD, ProEM-HS: 512 x 512, Princeton Instruments). This allows us to capture movies of each particle as it becomes trapped and its subsequent release. We provide one such example as Movie S1. In **Figure S6** of the Supporting Information, we show selected frames from this movie. The particle is initially trapped (Figure S6a, at t=7 s). The trapping laser is then turned off and the particle moves about randomly due to Brownian motion (Figure S6b, at t=11 s). The laser is then switched on again and the particle is again trapped (Figure S6c, at t=13 s).

Our direct observation approach allows us to record particle motion for trapping by the different aperture designs considered in this work. This allows us to find particle position distributions (**Figure 5a-c**) and effective trapping stiffnesses (Figure 5d-g). Using a particle detection algorithm,[55] we extract the particle position in the *x*-*y* plane from each movie frame for trapping with the DNH aperture, the SA aperture, and the SA2 aperture with ring coupler. Our experimental set-up does not allow direct measurement of the z-position. However, there is a strong correlation between z stiffness and x-y stiffness. We therefore conclude that while our experimental measurements are of the x-y stiffnesses, these results will suffice for the purpose of comparing and contrasting the trapping performance (i.e. x, y and z stiffnesses) of the different nanoaperture structures we consider in this study. One may also wonder whether the apertures will affect the emission pattern of the particle and thus influence its perceived position. However, the emission occurs at a wavelength in the visible (of ~575 nm) that is quite far from the aperture resonance (~1064 nm). The scattering of the particle emission by the aperture will therefore be non-resonant and is thus not expected to influence the perceived particle position

substantially. We further note that particle changes in brightness as a function of time (Movie S1). This is primarily due to it moving in the z-direction and the fairly shallow depth-of-field associated with our high numerical aperture lens. This change in brightness will not modify the centroid position as found by the particle tracking algorithm we use.

The results are plotted in Figure 5b. We separate these distributions into orthogonal components (i.e. along *x*- and *y*-axes) and plot the results, along with fitted Gaussians, as Figure 5a and c. We see that the optimized structure SA2 with rings confines the particle more tightly than the shaped aperture SA without the ring, and much more tightly than the original DNH.

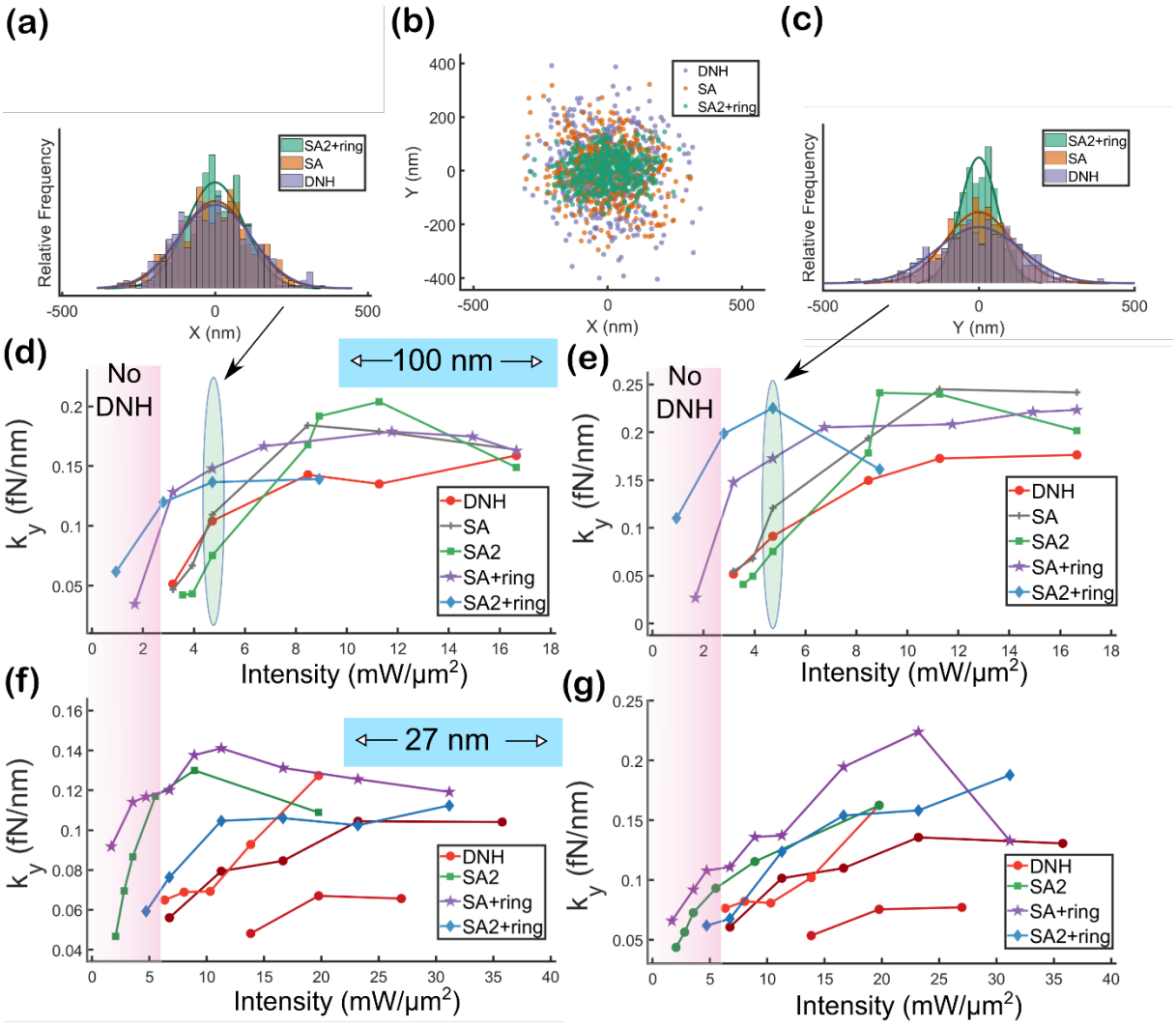

Figure 5: Experimental results. Laser wavelength is 1064 nm for all measurements. (a) x-position distribution, (c) y-position distribution, and (b) general position map of a trapped particle at a particular power level. (d-e) Estimated trap stiffness for the x and y directions respectively for 100 nm diameter particle. (f-g) Estimated trap stiffness for the x and y

directions respectively for 27 nm diameter particle. Note that along each connected red line trapping occurred with the same particle using DNH.

In addition to quantifying particle localization, the measured particle position distributions (Figure 5a-c) allow us to determine the effective trapping stiffnesses of the different plasmonic nanotweezers we consider. This is done by applying the equipartition theorem to yield the effective stiffness as $k_{stiff} = \frac{k_B T}{\Delta x^2}$, where k_B is Boltzmann's constant, T is temperature, and Δx is the standard deviation (along the x- or y-axis).[56,57] We apply motion blur correction to account for the finite integration time of the camera.[58] The results, i.e. along the *x*- and *y*-directions vs laser intensity for the different plasmonic nanotweezers considered, are provided as Figure 5d-g. As indicated, trapping is performed for nanoparticles with diameters of 100 nm and 27 nm. We note that laser intensity thresholds exist for trapping with the DNH, below which trapping is not observed. These thresholds are ~2.5 mW μm^{-2} for 100 nm diameter particles and ~6 mW μm^{-2} for 27 nm diameter particles (Figure 5d-g). For the optimized structures, trapping could still be observed for intensities down to 1 mW μm^{-2} for 100 nm diameter particles, and down to 2 mW μm^{-2} for 27 nm diameter particles. This demonstrates that the trapping performance of the algorithm-optimized structures are superior to that of the DNH. We also compare the measured particle distribution with the prediction of simulations in the Supporting Information (Figure 7-9).

The results demonstrate that the larger particles exhibit greater trapping stiffness. In addition, it can be seen that there is a positive correlation between laser power and trapping stiffness. We notice, however, that this effect saturates, plateauing for intensities exceeding ~10 mW μm^{-2}, a phenomenon also reported in other studies.[30] In Ref [30], this was attributed to convection currents resulting from heating. It would be interesting in future work to investigate this and other possible mechanisms such as the Soret effect (thermophoresis).[59]

3. Discussion

3.1. Spectral Investigation of Apertures

We next discuss the substantial enhancement of the electric field and optical force that our algorithm-designed nanoaperture exhibits in comparison with the starting DNH design (Figure 1b). To this end, we calculate the effective mode index vs wavelength of infinitely-long waveguides with the same cross sections as the DNH and SA2 designs. These allow us to identify the resonant wavelength of each aperture via the cut-off wavelength,[60] defined as when there is no propagation of the wave in the longitudinal direction, i.e. real part of the effective index of the mode reaches its minimum close to zero. This resonance has been associated with the zeroth order Fabry-Perot phase matching condition, which depends on the aperture geometry.[61,62] The results are plotted in **Figure S10**. The cut-off wavelength behavior is also shown to be consistent with the transmittance peak wavelength (**Figure S11**). From that figure, we find that the peak occurs at 1240 nm and ~ 1045 nm for the DNH and SA2, respectively. This indicates that the algorithm has shifted the resonant wavelength of the structure from 1240 nm to 1045 nm to closely match the excitation wavelength (of 1064 nm). We note that the cut-off wavelength is not expected to be precisely the same as the peak transmittance wavelength since this cut-off wavelength is obtained from an infinite waveguide model. The algorithm developed here can be useful in numerous applications in which plasmonic structures are designed to support resonances at target wavelengths. Examples include surface enhanced Raman scattering,[63] surface enhanced fluorescence,[64] plasmonic color filters for image sensors,[65] plasmonic color printing,[66] and plasmonic color holograms.[67]

As discussed, it is reasonable to conclude that the algorithm can find the shape that supports a resonance that matches the target wavelength. Along these lines, one might wonder whether the algorithm would produce an aperture with better performance if the operating wavelength were instead taken to match the DNH resonance (i.e. λ=1240 nm). To investigate this, we re-run our algorithm, this time at λ=1240 nm. The starting design is again taken as the DNH. The electric field enhancement plots for the DNH and for the algorithm-optimized apertures (SA3-5) are

shown as **Figure S12**. Here, we also investigate the effect of aperture shape by imposing different geometric constraints. For the SA2 design, the aperture shape is described by a curve that interpolates 14 points. For the SA3, SA4 and SA5 designs of Figure S12, the curves interpolate six, ten and 14 points, respectively. It can be seen that SA3-5 produce peak electric field enhancements (of ~22.6 to ~24.4) that surpass those of the DNH (~15.2). This confirms that the role of the algorithm is not solely that of resonance shifting. We further compare our algorithm-designed apertures to a DNH tuned to resonate at a wavelength of 1064 nm (**Figure S13**), like the optimized structure SA2. We can see that SA2 produces a peak electric field enhancement (~27) that still surpasses that of this DNH (~19.5) by ~40 percent.

4. Conclusion

Since their introduction more than a dozen years ago, optical nanotweezers based on plasmonic apertures have come to play a unique role in the field of nanoscience as a tool for the handling and sensing of nanomaterials. Early work was largely concerned with demonstrating that the trapping of nanoparticles was indeed possible.[11,22] This evolved to the trapping of ever-smaller particles (including single molecules),[12,35] to investigations aimed at better understanding the trapping process,[20,23,24] and to the demonstration of novel functionalities and approaches.[13,15,34,36,37] An on-going theme has also been the demonstration of new designs (i.e. new shapes) for plasmonic nanoapertures.[10,13,25,27–31] The design process has generally consisted of the researcher using physical intuition to choose the nanoaperture shape, followed by electromagnetic simulations to choose the dimensions (to maximize trapping performance). This leads to the question of whether an algorithmic approach might produce better results. Here we show that such an approach can indeed produce significantly improved trapping performance. We use an algorithm to design plasmonic nanoapertures and ring couplers, and nanofabricate them with helium and neon ion beams and compare them to a conventional design (double nanohole DNH). All the apertures are characterized by cathodoluminescence, and nanoparticle trapping is tested by experiment. Our results show that at every laser intensity, the

trapping performance of the DNH can be surpassed by that of an algorithm-optimized design. We anticipate that algorithmic approaches are also likely to benefit the design of other types of optical nanotweezers, e.g. those based on silicon photonics.

5. Methods

5.1. Algorithm Details

Electromagnetic simulations are performed in COMSOL Multiphysics v5.0 for every iteration of the algorithm, and the results are analyzed in MATLAB with the COMSOL LiveLink functionality. The shape is specified by twenty-four control points from which an interpolation curve is fitted to define the boundary. The simulation domain is enclosed by perfectly matched layers (PML) at the boundary, and we use a tetrahedral mesh throughout. The COMSOL built-in material catalogue is used for the optical properties of the simulations. In each iteration of the algorithm, one of these points is selected at random and has its position randomly shifted (within a specified radius). There are two sections around the gaps that are not allowed to change, to have a fair comparison between the original DNH and the optimized aperture. If this rule were not enforced, then the gaps could become arbitrarily sharp. The resultant (new) aperture shape is imported into COMSOL and the electric and magnetic fields are simulated. We use tetrahedral gridding, with a maximum dimension of 15 nm and a minimum dimension of 2 nm. From these, the Maxwell stress tensor (MST) is used to find the force on a particle (d= 10 nm, n = 1.6) near the aperture. Illumination is via a focused beam (NA = 1.3) which replicates the numerical aperture of the microscope objective in our experimental setup. The polarization is linear and across the aperture gap. The z-component of this force (i.e. that directing the particle into the aperture) is taken as the figure of merit (FOM) that the algorithm seeks to optimize. The algorithm compares the FOM of the present structure ($FOM_{current}$) to the preceding one ($FOM_{previous}$). If the performance of the present structure is better than that of its predecessor, the former is kept. If this is not the case, then a probability selection rule is used to determine whether the former is kept. This rule is as follows:

$$P_{keep\ current} = \begin{cases} 1, & FOM_{current} > FOM_{previous} \\ \left[1 + exp\left(\frac{FOM_{previous} - FOM_{current}}{T}\right)\right]^{-1}, & FOM_{current} < FOM_{previous} \end{cases} \quad (1)$$

The parameter *T* determines the acceptance probability of a structure with inferior performance. It is reduced as the algorithm progresses to facilitate the perturbations made to the aperture geometry being ever finer with iteration number.

The algorithm does not incorporate heat dissipation calculations. Rather, it enforces "broken" rings to make the metal film contiguous as this will ensure heat dissipation. We find that broken rings perform similarly to complete rings. This is because the gaps in the rings are small. These gaps are optimized for performance by the algorithm. Further simulations indicate that full rings with other depths (e.g. 80 nm) should produce stronger field enhancement. We do not implement these designs experimentally because we anticipate that the precise depth milling required might be difficult to achieve in practice. We thus use fully milled rings (i.e. through the film thickness) in experiments. This film thickness is 100 nm due to practical considerations (at the time that the experiment was performed, we had many glass slides onto which gold of this thickness had already been evaporated). It would be interesting in future work to re-optimize these designs, with the gold thickness allowed to vary.

5.2. Device Fabrication

Device shapes are compiled into a node list and exported to the software program (NPVE, Fibics Incorporated, Canada, version 4.8) used by the helium ion microscope (ORION NanoFab, Zeiss, Peabody MA). We first mill an array (3x3) of ring couplers (i.e. two rings of different radii), one by one. The rings are milled with a 20 keV Ne^+ beam, with typical beam current of 4 pA and with an aperture of diameter 20 μm. The beam dose, dwell time, and H/V spacing are 1 nC μm^{-2}, 1 μs and 0.25 nm, respectively. The beam is scanned left to right in a double serpentine pattern.

After the rings are milled, the apertures are milled with a 25 keV He^+ beam, with a typical beam current of 1 pA and with an aperture of diameter 10 μm. The beam dose, dwell time, and H/V spacing are 15 nC μm^{-2}, 1 μs and 0.25 nm, respectively. The beam is again scanned left to right in a double serpentine pattern.

5.3. Experimental Setup

A schematic of the experimental set-up is provided as Fig. 3b. We mount the sample, i.e. the microfluidic assembly, on an inverted microscope with the gold facing down. An oil immersion objective lens (numerical aperture NA=1.3, magnification=100X) is used to illuminate the sample with infrared (λ=1064 nm) and green (λ=532 nm) light for trapping and fluorescence excitation, respectively, and to collect the fluorescence emitted by the trapped nanoparticles. A half-wave plate and beam expander are used to control the polarization direction and to optimize the spot size, respectively, of the infrared trapping beam. Light from the green laser is passed through a ground glass diffuser to reduce speckle. It is furthermore focused with a lens, to ensure that it is not focused to a small spot by the microscope objective but instead illuminates an extended region so that the fluorescence microscopy of the nanoparticles (to be trapped) can be performed over that region. The fluorescent emission from the nanoparticles is collected by the microscope objective, passes through two short pass filters and is imaged onto the EMCCD camera with the microscope's tube lens system. A magnification of 150X is achieved. Each EMCCD pixel has a physical extent of 16 μm ×16 μm on the image sensor, which translate to 106.7 nm×106.7 nm at the sample.

5.4 Cathodoluminescence (CL) Measurements

CL measurements are performed on an FEI Nova NanoSEM using a 30 keV electron beam with a current of 4.9 nA. CL is collected in spectrum imaging mode, whereby a complete CL spectrum is acquired at every point in a scanned array. A Delmic SPARC CL system is used, equipped with an Andor Shamrock 303i spectrometer and Andor iVac spectral camera. The

beam current is kept constant for each specimen allowing qualitative comparison between the magnitude of CL emitted by the different apertures.

CL spectra are analyzed as follows. First a CL spectrum is measured from the sample at a location away from the nanoaperture. This is then regarded as the background and is thereafter subtracted from CL spectra measured from the aperture regions. Second, measured CL spectra are normalized against the detector spectral response that was determined from the transmission radiation spectrum of single crystal gold.[68] Spurious signals, e.g. from cosmic ray events, are removed.

Acknowledgements

The authors acknowledge use of facilities within the Monash Centre for Electron Microscopy. This work was performed in part at the Materials Characterisation and Fabrication Platform (MCFP) at the University of Melbourne and the Victorian Node of the Australian National Fabrication Facility (ANFF). This research used equipment funded by Australian Research Council (ARC, LE140100104). This work was furthermore supported by the ARC Discovery Projects scheme (DP180104141). AL acknowledges support from the Australian Research Council (FT180100594)

Conflict of Interest

The Authors declare no competing Conflict of Interest.

Contributions

N.L and K.C. designed the research; N.L. wrote the code for the algorithm and performed simulations of apertures; A.B performed the aperture fabrication; J.C aided the experimental setup; N.L. performed the experimental trapping measurements; A.L. performed the cathodoluminescence measurements and aided the analysis with N.L; A.R. performed mode analysis of the apertures; N.L., J.C., A.L., A.R., and K.C. analyzed and interpreted the results; N.L and K.C. wrote the paper. All authors edited and revised the paper and have given approval to its final version.

Supporting Information
Supporting Information is available from the Wiley Online Library or from the author.

References

[1] D.G. Grier, *Nature* **2003**, *424*, 810.

[2] M.-C. Zhong, X.-B. Wei, J.-H. Zhou, Z.-Q. Wang, Y.-M. Li, *Nat. Commun.* **2013**, *4*, 1768.

[3] D.G. Kotsifaki, S.N. Chormaic, (Preprint) arXiv:1905.10591v2, submitted: Jul **2019**

[4] K. Sasaki, M. Koshioka, H. Misawa, N. Kitamura, H. Masuhara, *Appl. Phys. Lett.* **1992**, *60*, 807.

[5] M.E.J. Friese, T.A. Nieminen, N.R. Heckenberg, H. Rubinsztein-Dunlop, *Nature* **1998**, *394*, 348.

[6] S.E.S. Spesyvtseva, K. Dholakia, *ACS Photonics* **2016**, *3*, 719.

[7] P.C. Chaumet, M. Nieto-Vesperinas, *Opt. Lett.* **2000**, *25*, 1065.

[8] D. Gao, W. Ding, M. Nieto-Vesperinas, X. Ding, M. Rahman, T. Zhang, C. Lim, C.-W. Qiu, *Light Sci. &Amp; Appl.* **2017**, *6*, e17039.

[9] P.J. Reece, *Nat. Photonics* **2008**, *2*, 333.

[10] A.A.E. Saleh, J.A. Dionne, *Nano Lett.* **2012,** *12*, 5581.

[11] M.L. Juan, M. Righini, R. Quidant, *Nat. Photonics* **2011**, *5*, 349.

[12] Y. Pang, R. Gordon, *Nano Lett.* **2011**, *11*, 3763.

[13] D. Yoo, K.L. Gurunatha, H.-K. Choi, D.A. Mohr, C.T. Ertsgaard, R. Gordon, S.-H Oh, *Nano Lett.* **2018**, *18*, 3637.

[14] A. Kotnala, D. DePaoli, R. Gordon, *Lab Chip* **2013**, *13*, 4142.

[15] Z. Xu, W. Song, K.B. Crozier, *ACS Photonics* **2018**, *5*, 2850.

[16] J.-S. Huang, Y.-T. Yang, *Nanomater.* **2015,** *5, 1048*.

[17] T. Shoji, Y. Tsuboi, *J. Phys. Chem. Lett.* **2014**, *5*, 2957.

[18] T. Rindzevicius, Y. Alaverdyan, B. Sepulveda, T. Pakizeh, M. Käll, R. Hillenbrand, J. Aizpurua, F.J. García de Abajo, *J. Phys. Chem. C* **2017**, *111*, 1207.

[19] C. Hong, S. Yang, J.C. Ndukaife, *Nat. Nanotechnol.* **2020***, 15, 908.*

[20] Q. Jiang, B. Rogez, J.-B. Claude, G. Baffou, J. Wenger, *ACS Photonics* **2019,** *6*, 1763.

[21] K. Wang, E. Schonbrun, P. Steinvurzel, K.B. Crozier, *Nat. Commun.* **2011**, *2*, 469.

[22] E.-S. Kwak, T.-D. Onuta, D. Amarie, R. Potyrailo, B. Stein, S.C. Jacobson, W.L. Schaich, B. Dragnea, *J. Phys. Chem. B* **2004**, *108*, 13607.

[23] P. Mestres, J. Berthelot, S.S. Aćimović, R. Quidant, *Light Sci. &Amp; Appl.* **2016***, 5*, e16092-.

[24] L. Neumeier, R. Quidant, D.E. Chang, *New J. Phys.* **2015**, *17*, 123008.

[25] C. Chen, M.L. Juan, Y. Li, G. Maes, G. Borghs, P. Van Dorpe, R. Quidant, *Nano Lett.* **2012**, *12*, 125.

[26] M.L. Juan, R. Gordon, Y. Pang, F. Eftekhari, R. Quidant, *Nat. Phys.* **2009**, *5*, 915.

[27] Y. Lin, P. Lee, *IEEE Photonics J.* **2019**, *11*, 1.

[28] K. Mokri, M.H. Mozaffari, *Opt. Laser Technol.* **2019**, *119*, 105620.

[29] R.A. Jensen, I.-C. Huang, O. Chen, J.T. Choy, T.S. Bischof, M. Lončar, M.G. Bawendi, *ACS Photonics* **2016**, *3*, 423.

[30] D.G. Kotsifaki, V.G. Truong, S.N. Chormaic, *Nano Lett.* **2020**, *20*, 3388

[31] T.D. Bouloumis, D.G. Kotsifaki, X. Han, S.N. Chormaic, V.G. Truong, *Nanotechnology* **2020**, *32*, 25507.

[32] M.A. Zaman, P. Padhy, L. Hesselink, *Sci. Rep.* **2019**, *9*, 649.

[33] Y. Zheng, J. Ryan, P. Hansen, Y.-T Cheng, T.-J Lu, L. Hesselink, *Nano Lett.* **2014**, *14*, 2971.

[34] A. Kotnala, R. Gordon, *Nano Lett.* **2014**, *14*, 853.

[35] Y. Pang, R. Gordon, *Nano Lett.* **2012**, *12*, 402.

[36] S. Wheaton, R.M. Gelfand, R. Gordon, *Nat. Photonics* **2015**, *9*, 68.

[37] J. Berthelot, S.S Aćimović, M.L. Juan, M.P. Kreuzer, J. Renger, R. Quidant, *Nat. Nanotechnol.* **2014**, *9*, 295.

[38] N. Li, J. Cadusch, K. Crozier, *Opt. Lett.* **2019**, *44*, 5250.

[39] B. Shen, P. Wang, R. Polson, R. Menon, *Nat. Photonics* **2015**, *9*, 378.

[40] J. Jiang, J.A. Fan, *Nano Lett.* **2019**, *19*, 5366.

[41] H. Chung, O.D. Miller, *Opt. Express* **2020**, *28*, 6945.

[42] P.J.M. van Laarhoven, E.H.L Aarts, in *Simulated Annealing: Theory and Applications* (eds.van Laarhoven, P.J.M., and Aarts, E.H.L.), Springer Netherlands, Dordrecht **1987**.

[43] S. Kirkpatrick, C.D. Gelatt, M.P. Vecchi, *Science* **1983**, *220*, 671.

[44] B.J.M. Brenny, T. Coenen, A. Polman, *J. Appl. Phys.* **2014**, *115*, 244307.

[45] M. Kociak, O. Stéphan, *Chem. Soc. Rev.* **2014**, *43*, 3865.

[46] E.J.R Vesseur, J. Aizpurua, T. Coenen, A. Reyes-Coronado, P.E. Batson, A. Polman, *MRS Bull.* **2012**, *37*, 752.

[47] B. Zhao, M.N. Lockrey, N. Wang, P. Caroff, X. Yuan, L. Li, J. Wong-Leung, H.H. Tan, C. Jagadish, *Nano Res.* **2020**, *13*, 2500.

[48] J.A. Lloyd, S.H. Ng, A.C.Y. Liu, Y. Zhu, W. Chao, T. Coenen, J. Etheridge, D.E. Gómez, U. Bach, *ACS Nano* **2017**, *11*, 1604.

[49] T.A. Gschneidtner, S. Lerch, E. Olsén, X. Wen, A.C.Y. Liu, A. Stolaś, J. Etheridge, E. Olsson, K. Moth-Poulsen, *Nanoscale* **2020**, *12*, 11297.

[50] T. Coenen, D.T. Schoen, S.A. Mann, S.R.K. Rodriguez, B.J.M. Brenny, A. Polman, M.L. Brongersma, *Nano Lett.* **2015**, *15*, 7666.

[51] A.C.Y. Liu, J. Lloyd, T. Coenen, D.E. Gómez, *Microsc. Microanal.* **2020**, *26*, 808.

[52] T. Coenen, E.J.R. Vesseur, A. Polman, *ACS Nano* **2012**, *6*, 1742.

[53] K. Singh, E. Panchenko, B. Nasr, A. Liu, L. Wesemann, T.J. Davis, A. Roberts, *Beilstein J. Nanotechnol.* **2018**, *9*, 1491.

[54] P. Chaturvedi, K.H. Hsu, A. Kumar, K.H. Fung, J.C. Mabon, N.C. Fang, *ACS Nano* **2009**, *3*, 2965.

[55] J.C. Crocker, D.G. Grier, *J. Colloid Interface Sci.* **1996**, *179*, 298.

[56] A. Rohrbach, *Phys. Rev. Lett.* **2005**, *95*, 168102.

[57] P.H. Jones, O.M. Maragò, G. Volpe, *Optical tweezers: Principles and applications*, Cambridge University Press, UK **2015**

[58] W.P. Wong, K. Halvorsen, *Opt. Express* **2006**, *14*, 12517.

[59] R. Piazza, *J. Phys. Condens. Matter* **2004**, *16*, S4195.

[60] I.A. Ibrahim, M. Mivelle, T. Grosjean, J.-T. Allegre, G.W. Burr, F.I. Baida, *Opt. Lett.* **2010**, *35*, 2448.

[61] H. Guo, T.P. Meyrath, T. Zentgraf, N. Liu, L. Fu, H. Schweizer, H. Giessen, *Opt. Express* **2008**, *16*, 7756.

[62] Y. Chen, A. Kotnala, L. Yu, J. Zhang, R. Gordon, *Opt. Express* **2015**, *23*, 30227.

[63] A.-I. Henry, T.W. Ueltschi, M.O. McAnally, R.P. Van Duyne, *Faraday Discuss.* **2017**, *205*, 9.

[64] E.C. Le Ru, P.G. Etchegoin, J. Grand, N. Félidj, J. Aubard, G. Lévi, *J. Phys. Chem. C* **2007**, *111*, 16076.

[65] S. Yokogawa, S.P. Burgos, H.A. Atwater, *Nano Lett.* **2012**, *12*, 4349.

[66] T.D. James, P. Mulvaney, A. Roberts, *Nano Lett.* **2016**, *16*, 3817.

[67] Y. Montelongo, J.O. Tenorio-Pearl, C. Williams, S. Zhang, W.I. Milne, T.D. Wilkinson, *Proc. Natl. Acad. Sci.* **2014**, *111*, 12679.

[68] T. Coenen, *PhD Thesis*, Universiteit van Amsterdam **2014**.

Table of Contents

Neuton Li, Jasper Cadusch, Amelia Liu, Anders J. Barlow, Ann Roberts, Kenneth B. Crozier**

Title

Algorithm-designed plasmonic nanotweezers: quantitative comparison by theory, cathodoluminescence and nanoparticle trapping

We use a simulated annealing optimization algorithm to design plasmonic apertures that have greater trapping performance than conventional aperture shapes. In addition, we use cathodoluminescence to investigate the spectral properties of the different apertures. With direct particle detection and tracking, we experimentally quantify trapping stiffness and demonstrate the superior performance of our designs.